2016

In situ measurements of plasma properties during gas-condensation of Cu nanoparticles

Mark A. Koten
University of Nebraska-Lincoln, mkoten2@unl.edu

S. A. Voeller
University of Wisconsin – Stout

M. M. Patterson
University of Wisconsin – Stout

Jeffrey E. Shield
University of Nebraska-Lincoln, jshield@unl.edu

JOURNAL OF APPLIED PHYSICS **119**, 114306 (2016)

In situ measurements of plasma properties during gas-condensation of Cu nanoparticles

M. A. Koten,[1,a)] S. A. Voeller,[2] M. M. Patterson,[2] and J. E. Shield[1]
[1]*Department of Mechanical and Materials Engineering, University of Nebraska, Lincoln, Nebraska 68588, USA*
[2]*Department of Chemistry and Physics, University of Wisconsin – Stout, Wisconsin's Polytechnic University, Menomonie, Wisconsin 54751, USA*

(Received 11 December 2015; accepted 28 February 2016; published online 16 March 2016)

Since the mean, standard deviation, and modality of nanoparticle size distributions can vary greatly between similar input conditions (e.g., power and gas flow rate), plasma diagnostics were carried out *in situ* using a double-sided, planar Langmuir probe to determine the effect the plasma has on the heating of clusters and their final size distributions. The formation of Cu nanoparticles was analyzed using cluster-plasma physics, which relates the processes of condensation and evaporation to internal plasma properties (e.g., electron temperature and density). Monitoring these plasma properties while depositing Cu nanoparticles with different size distributions revealed a negative correlation between average particle size and electron temperature. Furthermore, the modality of the size distributions also correlated with the modality of the electron energy distributions. It was found that the maximum cluster temperature reached during plasma heating and the material's evaporation point regulates the growth process inside the plasma. In the case of Cu, size distributions with average sizes of 8.2, 17.3, and 24.9 nm in diameter were monitored with the Langmuir probe, and from the measurements made, the cluster temperatures for each deposition were calculated to be 1028, 1009, and 863 K. These values are then compared with the onset evaporation temperature of particles of this size, which was estimated to be 1059, 1068, and 1071 K. Thus, when the cluster temperature is too close to the evaporation temperature, less particle growth occurs, resulting in the formation of smaller particles.
[http://dx.doi.org/10.1063/1.4943630]

I. INTRODUCTION

Clusters of atoms, alloy nanoparticles, and complex nanostructures have garnered much attention lately in the fields of electronics, semiconductors, biomagnetics, catalysis, and magnetism, because nanoscale materials and nanostructures exhibit different material properties from their bulk counterparts, which can influence functionality.[1–4] These structures and properties are often size dependent, and precise control over particle size, growth, and crystallization is critical for fabricating advanced nanostructures such as faceted, multiply twinned, chemically ordered, core-shell, onion-like, and hollow-shell geometries. Many of these structures are only possible within a narrow size range usually extending somewhere between 5 and 50 nm in diameter, while other structures exist in the molecular-cluster regime.[5–10] Similarly, the onset of surface atom effects occurs at particle sizes near or below about 2.5 nm in diameter.[11] In this size range, cluster properties can deviate from their bulk values towards the unexpected as quantum confinement of valence electrons or coordination-dependence can influence behavior, such as in the case of catalysis.[12] The growing interest in nanoparticles and clusters necessitates a more in-depth understanding of the fabrication methods that can be used to produce them. It further necessitates consistency in manufacturing and fabrication for different materials and alloys, such that the resulting nanostructures have the desired size, shape, and property profile.

Inert gas condensation (IGC) has become an increasingly popular method of producing clusters of atoms, nanoparticles, and complex nanostructures for a wide array of applications and fundamental cluster-science investigations.[11,13] However, challenges still exist in fine tuning particle sizes while maintaining narrow size distributions.[4] In the sub-2.5-nm regime, the difficulty lies in producing very small clusters with narrow size distributions, and sometimes clusters this small condense into highly disordered structures with poor crystallinity.[14,15] On the other hand, it is sometimes difficult to produce a narrow size distribution of particles that are larger than 20 nm without the use of a mass selection device, which greatly reduce deposition rates.[16–18] Additionally, the formation of bimodal size distributions is possible, but formation of such distributions is not well understood. Also not well understood is the heating of clusters during the growth stage as they pass through the densest part of the plasma. Many factors contribute to the particle size, including the erosion profile of the target, the processing parameters (buffer gas flow rate, sputtering power or pulse frequency, deposition rate, cooling liquid, chamber pressure), as well as the distance from the sputtering gun to the aperture.[19–22]

Yamamuro *et al.*[23] discovered that keeping the gas flow rate relatively low produces narrow size distributions in as-deposited nanoparticles. They attribute this to the prevention

a)Author to whom correspondence should be addressed. Electronic mail: mark.koten@gmail.com

of coagulation in the nucleation and growth regions. However, some peculiarities concerning the standard deviation and modality of nanoparticle size distributions produced by this method remain unexplained. They also found that the mean sizes of nanoparticle size distributions can be changed by varying the pressure in the condensation chamber (CC) while keeping the gas flow rate constant. Their method for doing so was to change the size of the exit orifice. The same procedure was followed here using three apertures of 2.5, 5.5, and 7.0 mm in diameter to produce three different depositions. Recent developments in the theory of cluster-plasmas have made it possible to investigate the role the plasma itself plays in the nucleation and growth process, and to this end, the plasma properties were measured *in situ* with the goal of finding the source of such variations in the nanoparticle size distributions.

II. EXPERIMENTAL PROCEDURE

A. Nanoparticle fabrication system

The IGC system used here is similar in design to those that have been cited in the literature[24–26] and contains both a condensation chamber and deposition chamber (DC) separated by two apertures. A notable difference is the absence of a mass selection device or aerodynamic lens system between the two chambers. The aperture that is nearest to the sputtering gun (Fig. 1 "A1") separates the condensation chamber from the rest of the machine and is the aperture that was changed in this study. The A2 aperture was fixed at 7.0 mm, but different A1 apertures were used for each deposition (7.0, 5.5, and 2.5 mm). For the purpose of this study, the DC sputtering gun (3 in. Stiletto series, AJA International) and Langmuir probe positions were fixed for

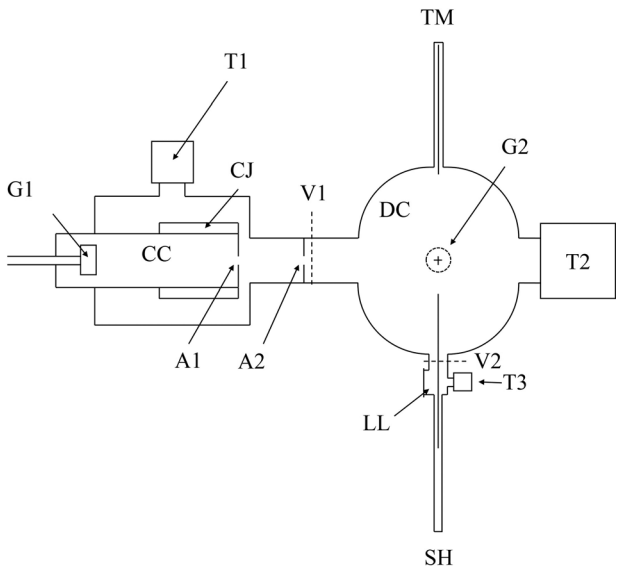

FIG. 1. An overhead diagram of the IGC cluster deposition system. The labels from left to right are as follows: (G1) DC sputtering gun, (T1) turbomolecular pump, CC, CJ, (A1) first aperture, (A2) second aperture, (V1) gate valve, DC, (TM) quartz crystal thickness monitor mounted on magnetic transfer rod, (G2) vertical RF sputtering gun, (V2) gate valve, (LL) load lock chamber, SH mounted on magnetic transfer rod, (T2, T3) turbomolecular pumps.

all measurements. The sputtering power was set to 100 W and the discharge current was roughly 350 mA. Water flowed through the cooling jacket (CJ) of the condensation chamber. As stated before, it is best if the flow rate of the argon (Ar) buffer gas remains low (<100 sccm for our system) and the deposition rates with the 2.5 and 5.5 mm aperture were 50 and 86 sccm. However, the rate for the 7.0 mm aperture was 186 sccm, which created a broader size distribution. The sputtering target was a 0.25 in. thick by 3 in. in diameter Cu disk (Kurt J. Lesker Company). A 2.5 nm carbon (C) film was also deposited for passivation and stabilization of the nanoparticles using the RF gun that is perpendicular to the DC gun but coincident with the substrate when the sample holder (SH) is inserted.

B. Langmuir probe setup and methodology

1. Design and position

To measure the plasma properties that might influence the heating and growth process, a Langmuir probe was fixed within the condensation chamber and was centered with respect to the aperture and sputtering gun. The probe consisted of tungsten (W) foil 12 mm in diameter that was soldered to a gold (Au) wire fed through a ceramic tube that electrically isolated the wire from ground. The W foil was oriented such that the planes of each face were perpendicular to the sputtering target face, which minimized both the amount of Cu deposited onto the foil and the effect of the magnetic field on the measured electron current.[27] The height of the probe was adjusted in the chamber so that the W collection area was positioned above the eroded ring or "racetrack," and the center of the probe was placed 1 cm from the surface of the Cu target inside the magnetic trap. A Keithley 2400 source/meter was configured to step voltage in the range of −40 to 14 V and measure the current in mA with a 0.5 s delay between the set point and measurement. The nanoparticles were deposited and then the probe current was measured as a function of step voltage immediately afterwards (without shutting off the sputtering gun and keeping all conditions the same as during the deposition).

2. Theory and analysis

Plasma diagnostics via Langmuir probes are a non-trivial way to obtain information about a plasma, particularly in the case of magnetron sputtering. However, the semiconductor industry has accumulated a great deal of experience and knowledge in this area over the past few decades. Here, the procedures outlined by Koo *et al.*[28] and Field *et al.*[29] were followed for the measurement of plasma potential (V_P), floating potential (V_f), electron temperature (T_e), and electron density (n_e). First, the ion contribution to the current was subtracted from the I-V trace by fitting the data in the ion saturation region and extrapolating to the plasma potential region. The two-tangent method for calculating V_P was employed, and the inverse of the slope in the region where the probe voltage is less than V_P was used to find T_e from the semilog plot of I-V. The electron density was then found from the following equation:[29]

$$n_e = \frac{I_e(V_P)}{eA_{col}}\sqrt{\frac{2\pi m_e}{kT_e}}, \quad (1)$$

where e is the elementary charge, m_e is the electron rest mass, A_{col} is the collection area of the probe, and $I_e(V_P)$ is the probe current at the plasma potential. In the case where two electron temperatures were observed, the effective electron temperature was approximated from the following equation:[28]

$$T_{eff} \cong \left(\frac{I_e^{*h}}{(T_e^h)^{1/2}} + \frac{I_e^{*c}}{(T_e^c)^{1/2}}\right) * \left(\frac{I_e^{*h}}{(T_e^h)^{3/2}} + \frac{I_e^{*c}}{(T_e^c)^{3/2}}\right)^{-1}, \quad (2)$$

where T_e^h, T_e^c, I_e^{*h}, and I_e^{*c} are the hot and cold electron temperatures and electron saturation currents, respectively. This value was then substituted into Eq. (1) to find the effective electron density n_{eff}.

C. Transmission electron microscopy (TEM)

The Cu nanoparticles were deposited onto Cu supported C films for imaging and analysis. An FEI Tecnai Osiris scanning transmission electron microscope (STEM) was used to image the particles at low magnification, selected area diffraction (SAD), and high resolution (HR). Fast Fourier transforms (FFTs) were also performed on the HR images. The sizes and size distributions were quantified in ImageJ, sampling approximately 800 nanoparticles for each data set.[30] These size distributions were then fitted by a Lorentzian function.

III. RESULTS AND DISCUSSION

A. Structure and size distributions

Three samples were made with different size distributions and were quantified in two ways using transmission electron microscopy. The first method measured the sizes directly from the bright-field TEM micrographs by setting a contrast threshold. Assuming spherical particles, their diameters D were calculated from their individual measured areas. Figure 2 shows the size distributions obtained for each deposition for the different apertures. The largest particles produced were made with the smallest aperture (2.5 mm), which produced an average size of 24.9 ± 3.8 nm. The smallest particles were produced with the largest aperture, but these particles also had a bimodal size distribution. To calculate the average sizes for this sample, the peaks were deconvoluted and fit independently for average sizes of 5.3 and 10.9 ± 1.1 nm. The mid-range aperture also had a size distribution (17.3 ± 2.4 nm) that fell in between these two extremes. The size distributions are also reasonably narrow as the ratio of the standard deviation to average size (σ/d) is less than 15% for all sizes except the smallest of the bimodal distribution where it is 20%. When viewed in this way, an inverse relationship appears to exist between the particle sizes and aperture diameter. However, this should not be interpreted as a direct result of changing the aperture, and

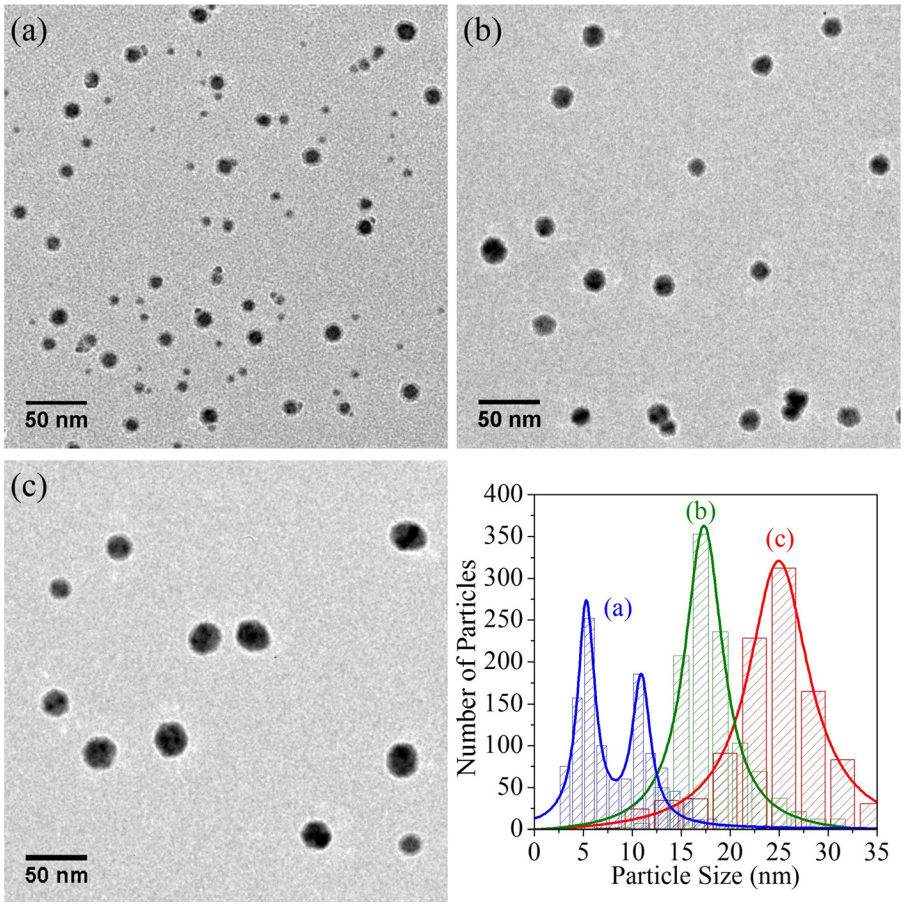

FIG. 2. TEM micrographs of as-deposited nanoparticles for (a) 7.0 mm, (b) 5.5 mm, and (c) 2.5 mm aperture. Particle size distributions for each sample.

other size distributions can be obtained for any given orifice diameter if different processing conditions are used. Thus, the orifice alone does not determine the final size distributions observed in Fig. 2, because those size distributions have been obtained at nearly optimal conditions. What governs the optimal conditions will be discussed in depth in Sec. III B.

The second method used to estimate the average sizes of the particles is based on the width of the intensity profile of the diffraction rings in polycrystalline diffraction patterns, which can be used as an inverse measure of grain size.[31] The particle diameter D was obtained from $D = 2w^{-1}$, where w is the full width of the peak at half the maximum measured in reciprocal space units. For this estimate, the {111} ring (Figs. 3(a)–3(c)) was normalized, and the intensity profile was obtained and is plotted in the inset of the SAD patterns. The particle sizes as calculated by this method were 8.2, 15.4, and 20.6 nm for the 7.0, 5.5, and 2.5 mm apertures, respectively. Each of these measurements is in good agreement with the measurements obtained from direct observation in the TEM except for that of the 2.5 mm aperture. This is because the sample produced with the 2.5 mm aperture had the fewest particles (about 30) inside the selected region, which resulted in a size distribution that was less accurate than the other two. This method also overlooks the bimodal size distribution, but reveals an accurate average of the total distribution in the particles produced with the 7.0 mm aperture.

Another consideration for formation and functionality of nanoparticles is crystallinity, which does not appear to be the same for each size range. Thus, the crystal quality of the various samples is compared through SAD patterns and high resolution imaging. The SAD aperture selects a region of the sample that is about 850 nm wide and 0.56 μm^2. Figure 2 shows that the number of clusters per area is not constant for each size distribution. This is because the amount of material deposited was held constant, but with the average particle size changing, the number of particles per unit area will vary between samples. Given the particle densities observed in Fig. 2, it is estimated that the number of particles sampled in the SAD patterns for the 8.2, 17.3, and 24.9 nm particle size distributions was 300, 70, and 30 nanoparticles, respectively. Although the ring intensity is related to the particle size, as discussed earlier, it should also be made up of discrete diffraction points. Figure 3(a) contains relatively few diffraction spots as compared to the other samples. One would expect that the SAD pattern containing 300 particles would have the most populated ring pattern compared to the one with only 30 particles, if all particles are crystalline. However, the trend observed in Figs. 3(a)–3(c) is the opposite. This suggests that per particle, the fraction of fully crystallized, well-formed particles is higher for the larger particle size distributions.

The HR images and the corresponding FFTs in Figs. 3(d)–3(f) provide more evidence that the crystal structure is more clearly defined in the larger particles than in the smaller ones. Each of these images shows a multiple twinned icosahedral Cu particle that is viewed along the three-fold symmetry axis. This structure was confirmed by measuring

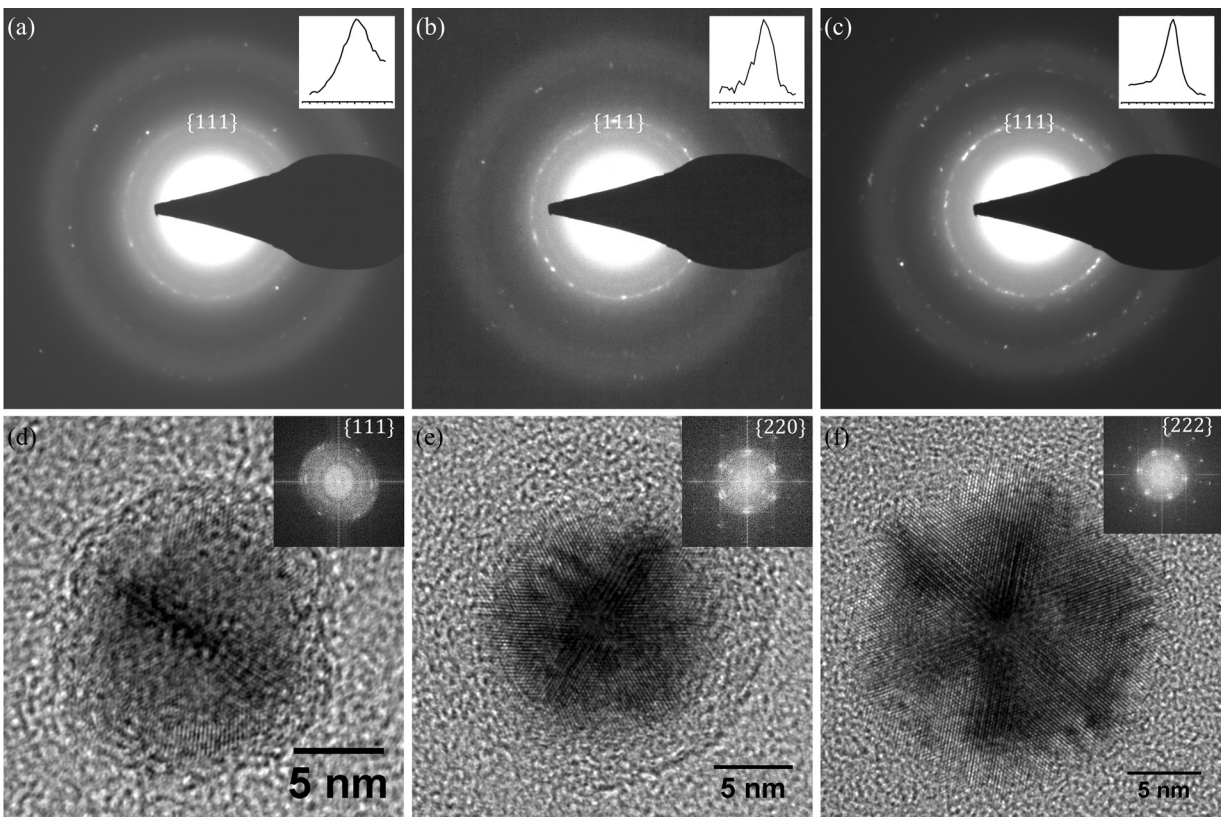

FIG. 3. TEM micrographs of the (a) and (d) 8.2, (b) and (e) 17.3, and (c) and (f) 24.9 nm particles. The insets of the SAD patterns (a), (b), and (c) show the intensity profile of the {111} ring. The insets in (d), (e), and (f) are the FFT of the HR image, and the highest-index set of reflections is listed. These images show atomic order increasing with particle size.

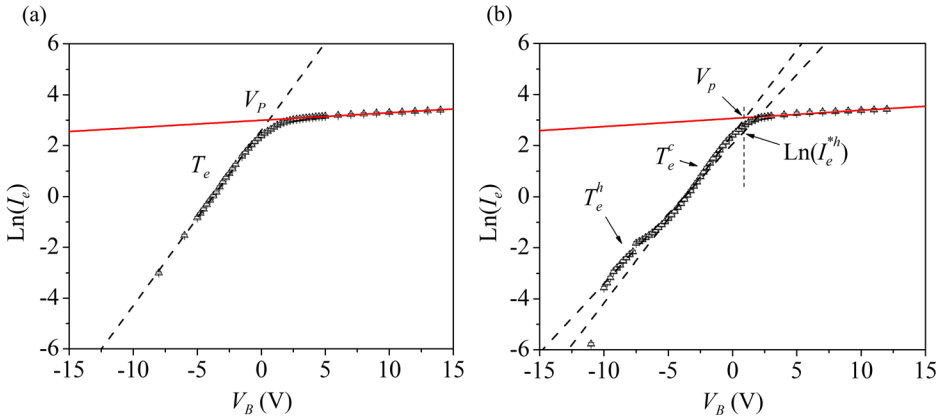

FIG. 4. Semi-log I-V plots obtained while depositing the (a) 17.3 nm and (b) 8.2 nm particles. The red line (solid) is the linear fit to the electron saturation region, and the black line (dashed) is the linear fit to the electron retardation region. The extra kink in (b) arises because there are two electron temperatures being measured in the probe at this region.

an angle of 60° between the six {111} reflections, which is not possible for the fcc structure except in the case of the multiple twinned icosahedron.[32] The lattice parameters were calculated from the {111} planes and were found to be 3.84 ± 0.23, 3.77 ± 0.19, and 3.62 ± 0.08 Å for the 8.2, 17.3, and 24.9 nm particles, respectively. Each of these values agrees reasonably well with the bulk value (3.61 Å), despite any size effects that may alter the lattice parameters.[33] This increase in lattice parameter may be caused by the lattice strain induced in the icosahedral volume, but one would expect this to be more constant since each size distribution has the same structure. The uncertainty decreases as smaller aperture sizes were used, which means the lattice parameters get more precise, and their accuracy was also improved with increasing particle size. Additionally, higher order planes were indexed in the inset FFTs of Figs. 3(d)–3(f). The highest indexed family of planes observed is labeled. This discussion indicates that the larger particles are more ordered and have better periodicity than the smaller particles, but icosahedra are usually less stable with increasing sizes.[11] This trend may be a result of the sputtering-based IGC processing route.

B. Plasma diagnostics

Due to recent advances in cluster-plasma theory,[38] the plasma properties were investigated with the goal of finding out how clusters of different sizes form under similar conditions. For each of the samples created above, a corresponding Langmuir probe trace was used to monitor the plasma properties of that deposition. This was then compared to the previously observed trends in particle size and crystallinity. Figure 4 demonstrates the graphical method used to calculate T_e and V_p from the raw Langmuir probe data. It also shows the difference in probe traces where the electron energy distribution is Maxwellian (Fig. 4(a)) and bi-Maxwellian (Fig. 4(b)). These semilog traces were made with the 5.5 and 7.0 mm apertures installed, and the 7.0 mm aperture produced a bimodal size distribution for this deposition. Thus, there may be a link between the dual electron temperatures and the bimodal size distributions.

The two-tangent method was performed by making two least-squares fits to the semilog I-V curve—one in the electron retardation region and one in the electron saturation region. The least-squares model was useful, because it allows for calculation of both the uncertainty in the measurement and the error in the fit parameters. The uncertainty in the measurement is shown as the error bars in Fig. 4, and the error in the fit parameters (Figs. 5 and 6), which were used to calculate values such as V_P and T_e, was propagated through the equations using standard error analysis rules.[34] Another advantage to this method is that it assigns weighted uncertainties to the measured values of I_e, which give a reasonable estimate of the uncertainty (±5%–10%) in the original measurement of current.

The electron temperatures measured in the condensation chamber were on the low end of the typical range (1 to 10 eV) measured for DC magnetron sputtering systems.[29] This was expected, because sputtering inside a condensation chamber occurs at a pressure that is a full order of magnitude higher than direct thin film sputtering. This reduces the mean free path and enhances the number of collision events between the various species in the discharge (ions, neutrals, and electrons). The increased collision events decrease the average energy of all species in the discharge, including electrons, lowering their temperature compared to traditional thin film sputter deposition. The values of T_e are plotted against particle size in Fig. 5. For the 24.9 and 17.3 nm distributions, these were found directly from the inverse

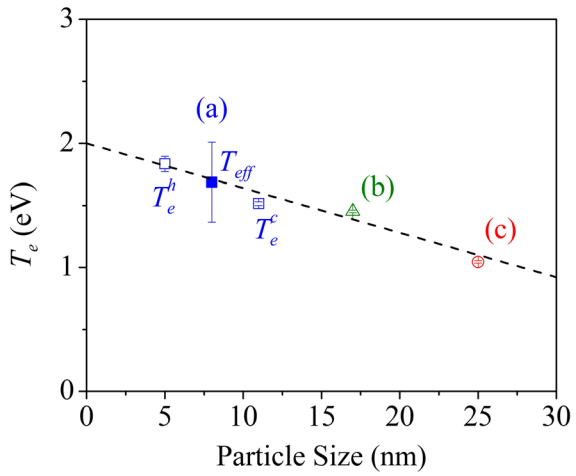

FIG. 5. Electron temperature as a function of particle size. The labels (a), (b), and (c) represent the 8.2, 17.3, and 24.9 nm distributions, respectively. The open squares are the components of T_{eff} for the bimodal size distribution. The dashed line serves as a guide to the eye.

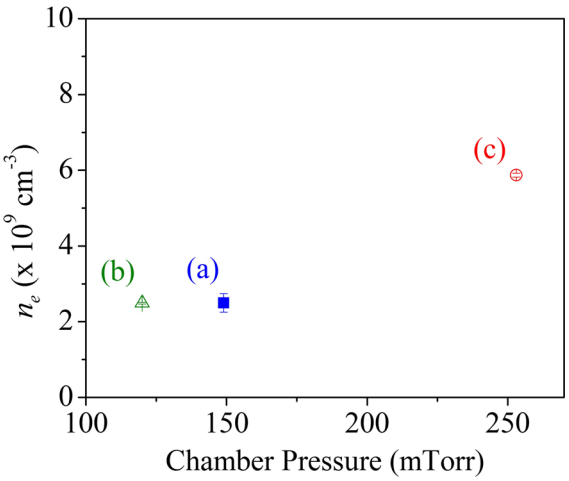

FIG. 6. Electron density versus pressure in the nucleation chamber for the (a) 8.2, (b) 17.3, (c) 24.9 nm distributions.

slope method. For the 8.2 nm particles, the inverse slope method was used to find T_e^h and T_e^c, and then Eq. (2) was used to calculate T_{eff}. I_e^{*h} was determined from the graph in Fig. 4(b) and $I_e^{*c} = I_e(V_P) - I_e^{*h}$. In Fig. 5, the T_{eff} of the bimodal size distribution falls in line with the other two aperture sizes. Furthermore, if T_e^h is assigned to the smaller of the two peaks and T_e^c is assigned to the larger, then the deconvoluted values of particle size also fall in line with this negative correlation.

Another important plasma property that was considered was the electron density. In a quasi-neutral plasma, the electron density can be assumed to be approximately equal to the ion density. In Fig. 6, a plot of the electron density versus chamber pressure shows that they may be proportional. This makes sense because the pressure is proportional to the neutral density, and in a weakly ionized plasma, n_i and n_e make up a very small fraction of the neutral density. However, the particle size does not appear to be strongly influenced by the chamber pressure or electron density. This can be seen for points (a) and (b) in Fig. 6, which were deposited at almost the same pressure and had similar electron densities, but very different size distributions. Thus, the electron temperature appears to be the parameter that is most intimately related to nanoparticle formation and can have an effect on both the crystal quality and particle size.

C. Calculating the cluster temperature

Two questions that arise from the data presented in Sec. III B are (1) how does the electron temperature affect the growth of a particle in the condensation chamber of an IGC system, and (2) how can this value be changed or controlled? The theory for nucleation and growth of clusters of atoms condensing out of the vapor state dates back to the 1970s and 1980s, when Hagena introduced his scaling laws that described the sizes of gas and metal clusters formed during free jet expansion through a nozzle into a vacuum chamber.[35,36] His empirically determined scaling laws successfully predicted cluster sizes based on the atomic number density, pressure, and temperature inside the chamber, as well as the nozzle diameter, by identifying a critical parameter that represented the ratio of the characteristic time for expansion to the time for cluster formation.[37] Therefore, the cluster size depends on this parameter under the right conditions. However, the Hagena parameter is not applicable to the plasma-based IGC method for two reasons. First, it was empirically determined for condensation processes in the absence of a plasma. Other treatments of condensation that neglect the cluster–plasma interactions, such as homogeneous nucleation theory, misrepresent this process primarily because of the fact that the clusters in the plasma acquire a net charge, which affects how they interact with other charged particles (i.e., electrons and ions). Second, the Hagena parameter is only applicable to the free jet expansion process, whereas during IGC, the clusters nucleate and grow before they are expanded through the aperture.

A successful representation of cluster–plasma systems has been achieved using Smirnov laws, which account for charge-effects in expressions for the rate of atom attachment to cluster surfaces and the amount of heat absorbed by the cluster through particle collisions. For the Cu clusters produced in this work, the cluster charge, which may be positive or negative, was calculated from the Langmuir probe data using Smirnov's expression for the average charge on a cluster interacting with a plasma[38]

$$\bar{Z} = 4\pi\varepsilon_o \frac{r_o T_e}{e^2}\left\{\ln\left[\frac{2}{n_e}\left(\frac{m_e T_e}{2\pi\hbar^2}\right)^{3/2}\right] - \frac{W}{T_e} - \frac{I-W}{T_e N^{1/3}}\right\}, \quad (3)$$

where I is the ionization potential and W is the work function (7.73, 4.4 eV for Cu) of the cluster material. The constant ε_o is the vacuum permittivity, r_o is the cluster radius as derived from the Wigner–Seitz model, $\hbar$ is the Plank's constant, and N is the number of atoms in the cluster. The average charge on the clusters is 125, 225, and 210 for the 8.2, 17.3, and 24.9 nm clusters, respectively. Each of these values is positive, which is in agreement with normal cluster production using this method.[39] This indicates that the many collisions with the electrons ionize less than 1% of the atoms inside the cluster.

The three temperatures that describe this system are the Ar gas temperature T, electron temperature T_e, and cluster temperature T_{cl}. The initial electron temperature near the sputtering target has been measured and discussed previously. The temperature of the Ar gas depends on the heat balance between the power supplied to the target that is lost to heat, which is estimated to be about 20% of the total power, and the wall temperature T_o. The temperature T_o depends on the cooling liquid, in this case water, so $T_o = 300$ K. The maximum temperature of the buffer gas can be simply calculated in temperature units for Ar by $T_{max} = 1.8 T_o Q^{0.57}$, where Q is the ratio of the power lost (20 W) to the chamber length (15 cm).[38] Therefore, $T \approx 0.055$ eV (636 K) for the buffer gas, which is two orders of magnitude lower than T_e. Since very little heat is exchanged between the buffer gas and the electrons in the plasma, the clusters will be heated by T_e and cooled by T, so $T < T_{cl} < T_e$. The cluster temperature can be approximated using Smirnov's relation $T_{cl} = (T + \xi T_e)\ (1+\xi)^{-1}$, where the coefficient ξ is described by[40]

$$\xi = \left(\frac{T_e m_a}{T m_e}\right)^{1/2}\left(1+\frac{\bar{Z}e^2}{4\pi\varepsilon_o r_o T_e}\right)\frac{n_e}{n_a}, \quad (4)$$

where m_a and m_e are the rest masses of the Ar atoms and electrons, respectively. The cluster temperatures for each sample at the location of the Langmuir probe can be obtained from this equation. Under these processing conditions, clusters of average sizes 8.2, 17.3, and 24.9 nm were heated to 0.089, 0.087, and 0.074 eV (corresponding to 1028, 1009, and 863 K, respectively). While the cluster temperature depends on several factors, including cluster size and charge, the primary source of heating is T_e, and as these clusters traverse the most intense region of the magnetron plasma, they are heated by the electrons to a value determined mostly by the electron temperature.

The kinetic definition of the cluster temperature can be defined as the sum of the rotational, translational, vibrational, and electronic energies. If the clusters are assumed to be rotationally and translationally frozen, then the internal energy $(3/2)T_{cl}$ can be equated with the average vibrational energy of the atoms that make up the cluster. This energy can be released through either collisions with the buffer gas, evaporation of atoms near the cluster surface, or through emission of electromagnetic radiation. Gspann calculated the power dissipated by radiation for a 3 nm cluster at 1500 K to be about 0.2 keV/s, and if the rate of evaporation of Cu atoms at 1500 K is combined with the typical heat of vaporization of 3.1 eV/atom, then the power dissipated by evaporation for a 3 nm cluster is about 6 keV/s, but this will increase dramatically for larger particle sizes.[41] Therefore, the radiation loss is negligible when compared to the heat lost through evaporation. Similarly, the power that the cluster loses to collisions with the buffer gas can be estimated by taking $(3/2)(T_{cl}-T)v_a n_a \sigma_a$, where υ_a and σ_a are the average velocities and collision cross sections of the buffer gas.[40] This gives an estimate of about 1 MeV/s, for the temperatures and densities used in this work, and is in agreement with the available litterature.[42] A similar equation estimates a 3 nm cluster gains energy at a rate of about 40 keV/s from the collisions with the plasma's electrons. Thus, the internal energy of the clusters is reduced mostly through collisions with the buffer gas.

Within the framework of the liquid drop model, an expression can be obtained for the equilibrium temperature T_{eq} between the condensation and evaporation processes. At this temperature, the rates of atom attachment to the cluster surface and evaporation from the surface will be equal for a given particle size and number density. At temperatures greater than T_{eq}, the rate of evaporation will exceed the rate of attachment. Thus, if $T_{cl} \approx T_{eq}$, particle growth will cease. The equilibrium temperature can be obtained from[38]

$$T_{eq} = \left(-\frac{2A}{3N^{1/3}}+\varepsilon_b\right)\left(\ln\frac{n_o}{n}\right)^{-1}, \quad (5)$$

where A and ε_b are the specific surface energy and bulk binding energy per atom (2.2, and 3.4 eV for Cu), respectively. The parameter n is the number density of Cu atoms in the chamber, and n_o is the pre-exponential factor found in the rate equation for the number density at the saturation vapor pressure ($8.33 \times 10^{24}\,\mathrm{cm}^{-3}$). From this model, the equilibrium temperatures for 8.2, 17.3, and 24.9 nm clusters were found to be about 1060, 1068, and 1071 K. When compared with their respective cluster temperatures, it is interesting to note that the smaller particles have temperatures that are very close to this threshold.

This discussion offers some idea of the role, the plasma characteristics, and the material properties of the target play in cluster formation. Atoms that are sputtered from the surface typically leave with about 1–10 eV of energy.[43,44] These atoms are cooled by the inert gas at a rate of 1 MeV/s until their temperatures fall below the evaporation/condensation threshold, and they then begin to condense into clusters. As they pass by the Langmuir probe, we can measure their temperatures, and we found them to be a few hundred Kelvin above the temperature of the buffer gas. Depending on the electron temperature, some of the clusters remain closer to the condensation/evaporation threshold than others, and these clusters do not grow as large because their growth is inhibited by evaporation.

This analysis supports the idea that particle growth depends on the electron temperature, which can influence the final size distribution in several ways (i.e., peak position, standard deviation, and modality). T_e depends approximately on the ratio V/p, where V is the voltage applied to the sputtering target and p is the chamber pressure.[45,46] Therefore, it may be possible to monitor the relative value of T_e through comparison of external parameters such as voltage and pressure, which are often monitored during nanoparticle deposition. For the three depositions produced here, the values of (V/p) were 1.1, 2.4, and 1.9 V/mtorr, and the values of T_e for each deposition were (a) 1.04, (b) 1.45, and (c) 1.68 eV. The lowest ratio of V to p corresponds to the lowest T_e observed in the plasma, while the highest value does not correspond to the highest T_e, although the presence of a bimodal size distribution and two electron temperatures in the sample with the highest T_e might make for a bad example. Nevertheless, this ratio is a crude marker, but it should also be noted that in this experiment, power was held constant, and voltage and pressure varied slightly between deposition, perhaps keeping the pressure constant and varying voltage would make for a better evaluation of the relationship between T_e and V/p.

IV. CONCLUSION

Nanoparticles of many shapes and geometries that form in different size ranges require precise control over the size distributions of as-deposited materials. Here, pure Cu nanoparticles that ranged from 5 to 25 nm were produced in a sputtering-based IGC system. Their sizes and structures were determined using transmission electron microscopy, and it was found that they form in multiple twinned icosahedral structures. Additionally, the crystal quality was observed to be better in the larger particles than in the smaller particles.

In situ measurements of the plasma properties during the deposition of different size distributions revealed a negative correlation between particle size and electron temperature. Analysis of the cluster–plasma system suggests that the

clusters are heated through collisions with the plasma's electrons and cooled through collisions with the inert gas atoms. This is because the average charge on the clusters is positive, which increases their attraction to free electrons and also increases the number of electron–cluster collisions. It was also found that plasmas with two T_e's coincide with bimodal size distributions. This happened in the sample that was deposited at a higher Ar flow rate, which may have initially created a distribution with a large standard deviation. During the growth stage, this may have been converted into a bimodal size distribution through cluster heating via the two electron temperatures.

Since the sputtered Cu atoms are essentially being quenched rapidly by the Ar gas throughout their time in the condensation chamber, the plasma serves as a heating source that can delay this quenching process and possibly even reverse it depending on the electron density. The temperature that the clusters are held at while they pass through the plasma depends on the electron temperature, and it seems lower electron temperatures lead to cluster temperatures of about 860 K, which is ideal for forming Cu nanoparticles of 25 nm. If the clusters spend too much time near their evaporation temperatures, growth can be interrupted, and the result is smaller particles. As the particles exit the plasma, they undergo another stage of quenching. Quenching from higher temperatures can result in poorly formed or even amorphous nanoparticles. Thus, fabrication of nanoparticles in plasmas with high electron temperatures may prevent the formation of large particles and crystalline structures. On the other hand, keeping the electron temperature low may allow for sustained growth and slower cooling rates, because the cluster temperature stays below the evaporation threshold resulting in particles that are larger and crystalline.

ACKNOWLEDGMENTS

This work was financially supported by the U.S. NSF-MPS-DMR (Grant No. 0820521, Program Director D. Finotello) and the Robert W. Brightfelt Fellowship. Research was performed in the facilities of the Nebraska Center for Materials and Nanoscience, which are supported by the Nebraska Research Initiative. With special thanks to Professor N. J. Ianno for helpful discussions.

[1]R. Ferrando, J. Jellinek, and R. L. Johnston, Chem. Rev. **108**, 845 (2008).
[2]J. Jortner, Z. Phys. D: At. Mol. Clusters **24**, 247 (1992).
[3]R. G. Chaudhuri and S. Paria, Chem. Rev. **112**, 2373 (2012).
[4]R. L. Johnston, Philos. Trans. R. Soc. London, Ser. A **356**, 211 (1998).
[5]T. Shibata, B. Bunker, Z. Zhang, D. Meisel, C. F. Vardeman, and J. D. Gezelter, J. Am. Chem. Soc. **124**, 11989 (2002).
[6]S. Stappert, B. Rellinghaus, M. Acet, and E. F. Wassermann, J. Cryst. Growth **252**, 440 (2003).
[7]D. Reinhard, B. Hall, P. Berthoud, S. Valkealahti, and R. Monot, Phys. Rev. Lett. **79**, 1459 (1997).
[8]D. Reinhard, B. Hall, P. Berthoud, S. Valkealahti, and R. Monot, Phys. Rev. B **58**, 4917 (1998).
[9]T. P. Martin, Solid State Ionics **131**, 3 (2000).
[10]W. D. Knight, K. Clemenger, W. A. de Heer, W. A. Saunders, M. Y. Chou, and M. L. Cohen, Phys. Rev. Lett. **52**, 2141 (1984).
[11]F. Baletto and R. Ferrando, Rev. Mod. Phys. **77**, 371 (2005).
[12]E. Roduner, Chem. Soc. Rev. **35**, 583 (2006).
[13]F. E. Kruis, H. Fissan, and A. Peled, J. Aerosol Sci. **29**, 511 (1998).
[14]E. Quesnel, E. Pauliac-Vaujour, and V. Muffato, J. Appl. Phys. **107**, 054309 (2010).
[15]J. G. Lee, H. Mori, and H. Yasuda, J. Mater. Res. **20**, 1708 (2005).
[16]M. Gracia-Pinilla, E. Martínez, G. S. Vidaurri, and E. Pérez-Tijerina, Nanoscale Res. Lett. **5**, 180 (2009).
[17]R. M. Nielsen, S. Murphy, C. Strebel, M. Johansson, I. Chorkendorff, and J. H. Nielsen, J. Nanopart. Res. **12**, 1249 (2010).
[18]J. Kousal, O. Polonskyi, O. Kylián, A. Choukourov, A. Artemenko, J. Pešička, D. Slavínská, and H. Biederman, Vacuum **96**, 32 (2013).
[19]M. Ganeva, A. V. Pipa, and R. Hippler, Surf. Coat. Technol. **213**, 41 (2012).
[20]M. Ruano, L. Martínez, and Y. Huttel, Dataset Papers in Science **2013**, 1.
[21]L. Martínez, M. Diaz, E. Román, M. Ruano, D. P. Llamosa, and Y. Huttel, Langmuir **28**, 11241 (2012).
[22]R. Werner, T. Höche, and S. G. Mayr, CrystEngComm **13**, 3046 (2011).
[23]S. Yamamuro, K. Sumiyama, and K. Suzuki, J. Appl. Phys. **85**, 483 (1999).
[24]H. Haberland, M. Karrais, M. Mall, and Y. Thurner, J. Vac. Sci. Technol., A **10**, 3266 (1992).
[25]S. H. Baker, S. C. Thornton, K. W. Edmonds, M. J. Maher, C. Norris, and C. Binns, Rev. Sci. Instrum. **71**, 3178 (2000).
[26]C. Binns, Surf. Sci. Rep. **44**, 1 (2001).
[27]E. Passoth, P. Kudrna, C. Csambal, J. F. Behnke, M. Tichy, and V. Helbig, J. Phys. D: Appl. Phys. **30**, 1763 (1997).
[28]B. W. Koo, N. Hershkowitz, and M. Sarfaty, J. Appl. Phys. **86**, 1213 (1999).
[29]D. J. Field, S. K. Dew, and R. E. Burrell, J. Vac. Sci. Technol., A **20**, 2032 (2002).
[30]C. A. Schneider, W. S. Rasband, and K. W. Eliceiri, Nat. Methods **9**, 671 (2012).
[31]D. B. Williams and C. B. Carter, *Transmission Electron Microscopy Part 2: Diffraction* (Springer Science+Business Media, LLC, New York, NY, 2009), Vol. 2.
[32]P.-A. Buffat, M. Flueli, R. Spycher, P. Stadelmann, and J.-P. Borel, Faraday Discuss. **92**, 173 (1991).
[33]P. Villars, *Pearson's Handbook Desk Edition Crystallographic Data for Intermetallic Phases* (ASM International, 1997), Vol. 2.
[34]J. R. Taylor, *An Introduction to Error Analysis*, 2nd ed. (University Science Books, Suusalito, CA, 1997).
[35]O. F. Hagena, Phys. Fluids **17**, 894 (1974).
[36]O. F. Hagena, Z. Phys. D: At. Mol. Clusters **4**, 291 (1987).
[37]B. M. Smirnov, Phys. Scr. **50**, 364 (1994).
[38]B. M. Smirnov, *Cluster Processes in Gases and Plasmas* (WILEY-VCH Verlag GmbH & Co. KGaA, Weinheim, Germany, 2010).
[39]B. M. Smirnov, I. Shyjumon, and R. Hippler, Phys. Rev. E: Stat. Phys. Plasmas Fluids Relat. Interdiscip. Top. **75**, 066402 (2007).
[40]B. M. Smirnov, Phys. Usp. **40**, 1117 (1997).
[41]J. Gspann, Z. Phys. D: At. Mol. Clusters **3**, 143 (1986).
[42]J. Zhao, V. Singh, P. Grammatikopoulos, C. Cassidy, K. Aranishi, M. Sowwan, K. Nordlund, and F. Djurabekova, Phys. Rev. B **91**, 035419 (2015).
[43]P. Sigmund, Thin Solid Films **520**, 6031 (2012).
[44]J. Lu and C. G. Lee, Vacuum **86**, 1134 (2012).
[45]F. F. Chen and J. P. Chang, *Lecture Notes on Principles of Plasma Processing* (Plenum/Kluwer Publishers, New York, 2003).
[46]H. Dreicer, Phys. Rev. **117**, 343 (1960).